A generic high-throughput microstructure classification and quantification method for regular SEM images of complex steel microstructures combining EBSD labeling and deep learning

Shen, Chunguang; Wang, Chenchong; Huang, Minghao; Xu, Ning; van der Zwaag, Sybrand; Xu, Wei

DOI
10.1016/j.jmst.2021.04.009

Publication date
2021

Document Version
Final published version

Published in
Journal of Materials Science and Technology

Citation (APA)
Shen, C., Wang, C., Huang, M., Xu, N., van der Zwaag, S., & Xu, W. (2021). A generic high-throughput microstructure classification and quantification method for regular SEM images of complex steel microstructures combining EBSD labeling and deep learning. *Journal of Materials Science and Technology*, *93*, 191-204. https://doi.org/10.1016/j.jmst.2021.04.009

Journal of Materials Science & Technology 93 (2021) 191–204

Contents lists available at ScienceDirect

Journal of Materials Science & Technology

journal homepage: www.elsevier.com/locate/jmst

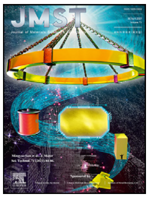

Research Article

A generic high-throughput microstructure classification and quantification method for regular SEM images of complex steel microstructures combining EBSD labeling and deep learning

Chunguang Shen[a], Chenchong Wang[a,*], Minghao Huang[a], Ning Xu[a], Sybrand van der Zwaag[b], Wei Xu[a,*]

[a] State key laboratory of rolling and automation, Northeastern University, Shenyang, Liaoning 110819, China
[b] Novel Aerospace Materials Group, Faculty of Aerospace Engineering, Delft University of Technology, 2629 HS Delft, the Netherlands

ARTICLE INFO

Article history:
Received 1 February 2021
Revised 17 March 2021
Accepted 7 April 2021
Available online 11 May 2021

Keywords:
Microstructure quantification
Deep learning
Electron backscatter diffraction
Small sample problem

ABSTRACT

We present an electron backscattered diffraction (EBSD)-trained deep learning (DL) method integrating traditional material characterization informatics and artificial intelligence for a more accurate classification and quantification of complex microstructures using only regular scanning electron microscope (SEM) images. In this method, EBSD analysis is applied to produce accurate ground truth data for guiding the DL model training. An U-Net architecture is used to establish the correlation between SEM input images and EBSD ground truth data using only small experimental datasets. The proposed method is successfully applied to two engineering steels with complex microstructures, i.e., a dual-phase (DP) steel and a quenching and partitioning (Q&P) steel, to segment different phases and quantify phase content and grain size. Alternatively, once properly trained the method can also produce quasi-EBSD maps by inputting regular SEM images. The good generality of the trained models is demonstrated by using DP and Q&P steels not associated with the model training. Finally, the method is applied to SEM images with various states, i.e., different imaging modes, image qualities and magnifications, demonstrating its good robustness and strong application ability. Furthermore, the visualization of feature maps during the segmenting process is utilised to explain the mechanism of this method's good performance.

1. Introduction

Microstructure classification and quantification act as a bridge between chemical composition, processing conditions and mechanical properties and hence it is crucial in the development of new metals and physical metallurgy models for microstructure evolution [1–3]. When developing metallic materials (or other materials with a well-defined microstructure) via purely experimental routes, it is essential to build quantitative "microstructure/property" correlations and explore the physical mechanism underlying these correlations [4]. Alternatively, for development of new materials based on integrated computational materials engineering (ICME) or methods from the materials genome initiative (MGI), inclusion of quantitative microstructural information of existing materials into a computational framework is also very important to enhance the robustness of the model and to be able to backtrack "microstructure/property" relationships [5,6]. In order to meet the request for metals with extremely good mechanical properties the microstructures of various metallic materials have become increasingly more complicated. Complex microstructures can exhibit improved mechanical properties but they also make it increasingly difficult to quantify them properly, which limits the further development of MGI using quantitative microstructural information. Traditionally, microstructures were observed via optical microscopy (OM) and some rough first-order quantitative analyses were performed using software based on image statistics [7]. However, this method can only apply reliably to simple microstructures, and any quantitative data extracted from these images is closely related to the operator's experience or the set threshold values in the image analysis. While optical microscopy certainly has its attractive features, for more complex microstructures with micron-sized dimensions, higher resolution electronic imaging techniques are required [8–10]. For example, high-resolution SEM has become the common approach for recording the detailed features of dif-

---

[*] Corresponding authors.

E-mail addresses: shenchunguang@stumail.neu.edu.cn (C. Shen), wangchenchong@ral.neu.edu.cn (C. Wang), 1710215@stu.neu.edu.cn (M. Huang), xun0909@stumail.neu.edu.cn (N. Xu), S.vanderZwaag@tudelft.nl (S. van der Zwaag), xuwei@ral.neu.edu.cn (W. Xu).

https://doi.org/10.1016/j.jmst.2021.04.009
1005-0302/© 2021 Published by Elsevier Ltd on behalf of Chinese Society for Metals.

ferent phases and phase classification [11,12]. Moreover, quantitative analysis of microstructures can also be performed based on SEM images. Medinaa et al. quantified the various kinds of phases in DP600 steel based on SEM images using conventional image analysis software [13]. However, this method often yielded semi-accurate results because the software parameters were set by the operator. Taillon et al. acquired more accurate quantitative microstructural information for solid oxide fuel cell cathode samples (e.g., overall porosity and tortuosity) based on advanced FIB/SEM nanotomography [14], but the enormous time and funding costs of such experiments limits their efficiency and large-scale application. Although microstructures are regularly characterized and quantified using SEM images, the method has some intrinsic limitations: (i) an SEM image provides contrast information as the morphology, making it difficult to apply SEM to complex microstructures in which phase boundaries are sometimes not observable and the pattern depends on the etching conditions; and (ii) quantification of the microstructural components usually requires time-consuming experiments combined with image processing software that utilizes human intervention. Notwithstanding its limitation in accuracy and reproducibility, SEM in combination with image analysis remains an interesting technique as it is fast and hence relatively cheap and can be applied to scan larger surfaces at adjustable and appropriate magnifications.

To overcome the limitations mentioned above, two research directions for quantitative metallography have been developed over recent years. Some studies focused on the limits of the contrast information itself. However, the morphology or contrast information provided by SEM intrinsically is not the most accurate information to distinguish phases and dimensions of microstructural entities. Such information only can come from measurements revealing the local crystal structure and orientation. Therefore, EBSD techniques have grown to become a powerful tool for both microstructure classification and quantification [15–18]. Various complex microstructures in common steels have been accurately identified by EBSD methods [19–21]. For example, Ryde was successfully classified bainite, ferrite, martensite and retained austenite (RA) in sheet steel, showing the unique advantages in classifying complex microstructures [20]. However, often a relatively small step size, e.g., less than 0.1 μm, is required to acquire sufficiently detailed information to accurately classify microstructures, making the technique time consuming and expensive, limiting its application [22]. Recently, Gaskey et al. developed a novel approach to produce the crystal orientation map using nothing more than a conventional OM image and a commercial laptop, which greatly expanded applicability and broadened access [23]. However, this approach was only suitable to capture large-scale (>100 μm) features, and is not suitable for multiphase steels with micron-scale microstructures.

In order to reduce the time and hence the costs required for microstructure classification and quantification, a more generic and effective method capable of handling with micron- and sub-micron scale dimensions is required. With the rapid development of data-driven artificial intelligence (AI) techniques in the field of materials science, research has focused on methods of identifying phases on the basis of morphology information. In contrast to the first approach, which focused on just the morphology information itself, this second approach still uses morphology information as the sole input, but uses AI techniques instead of human experience to extract the morphological features. Because they have more powerful and reproducible segmentation and analysis abilities than the human brain, AI techniques effectively reduce the level of artificial errors during microstructure classification of various metal materials and do so at an extremely low time cost. Using conventional machine learning (ML) methods, Gola et al. applied a support vector machine (SVM) to successfully classify microstructures in dual-phase steel with acceptable accuracy [24,25]. Decost et al. classified microstructures in various types of materials using an SVM (e.g., brass and ductile cast iron), showing the high efficiency of this technique [26]. However, these studies classified microstructures using only visual micrographic input features, which implies rather incomplete descriptions in case of comprehensive microstructures and limits the predicted accuracy. In the last decade, DL methods have rapidly developed that outperform conventional ML [27,28], especially on image segmentation tasks. Considering their excellent performance, advanced DL approaches have been widely applied in a variety of research fields, e.g., autonomous driving [29,30], health care [31,32] and intelligent transportation [33,34]. Additionally, DL methods for microstructure segmentation and further quantification have gathered attention in the material science community [35–38]. Azimi et al. performed pixelwise segmentation of low carbon steel microstructures in SEM images by employing a fully convolutional neural network (FCNN), enabling them to segment martensite in a ferrite matrix [35]. However, this work required a large dataset: 21 large-size images with 7000 × 8000 pixels were used to train the model, and equally important to state, the ground truth labels were annotated manually. Ajioka et al. applied the U-Net architecture to successfully classify simple microstructures in DP steel (ferrite and martensite) using 40 images (1536 × 1536 pixels) again with manual ground truth, demonstrating that this model is also applicable to relatively small samples [36]. To achieve further quantification, DeCost et al. applied the segmentation model to obtain various types of quantitative microstructural information for ultrahigh carbon steel, but this study also used manually (and subjectively) produced ground truth data to train the network [38]. Although rapid microstructure classification and quantitation via DL methods have been successfully performed, due to the limitation of manual annotation most of them were applied to steels with relatively simple microstructures. Recently, Müller et al. [39] proposed that material knowledge is indispensable for building a high-quality ML-based segmentation method, and in their work a correlative characterization using OM, SEM and EBSD was successfully applied to annotate complex microstructure. e.g., bainite. Moreover, in most researches, DL models were only available to high-quality images taken under the same conditions (magnification, resolution, etc.) as those used in model training. However, in practice, the image quality may change due to changes in experimental conditions and often the images are taken at different magnifications to optimally observe the different microstructural features. Thus, a genetic DL-based method suitable to analyze images taken under different imaging conditions is also needed.

In present work, an EBSD-trained DL method is proposed to establish a generic, robust and low-cost framework for classifying and quantifying complex microstructures only using regular SEM images. The proposed method uses a small number of EBSD maps to form the ground truth of SEM images and then applies a popular U-Net architecture to learn the high-order features and perform a pixelwise segmentation of the input SEM images, and finally obtain quantitative microstructural information via pixel statistics using the OpenCV package [40]. Based on the method to be described, complex microstructures of two common engineering steels, a DP steel and a Q&P steel, were segmented and quantified, and quasi-EBSD maps can be produced using regular SEM images. Additionally, this method was also applied to low-quality images and images with different magnifications, to reveal its robustness and applicability in real-world scenarios.

2. Methodology

The schematic diagram of the present method is shown in Fig. 1. The available inputs come from two engineering steels with a complex microstructure, i.e., a DP steel (austenite and marten-

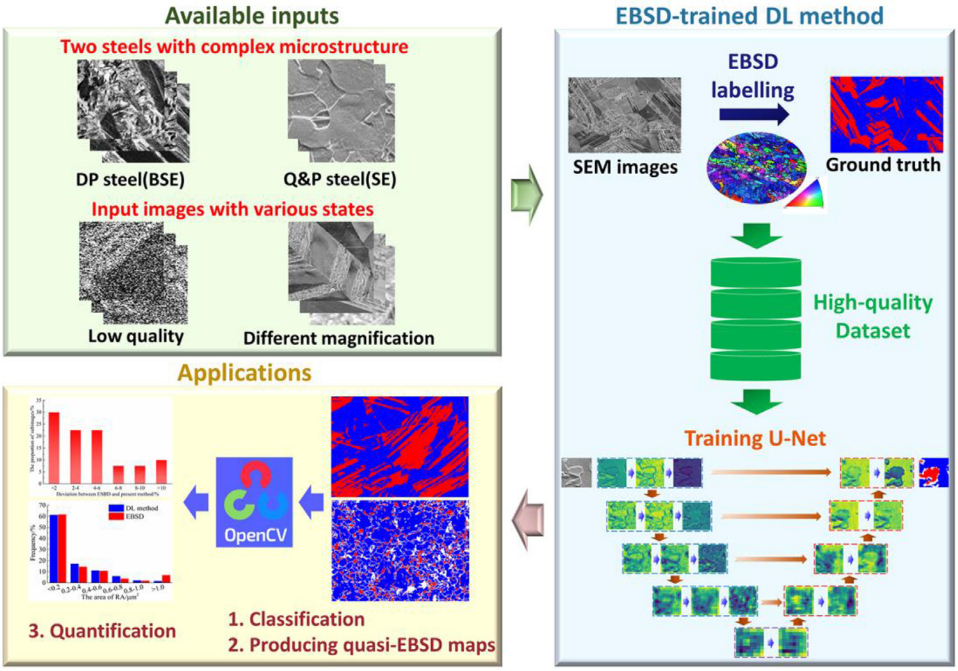

Fig. 1. The schematic diagram of the EBSD-trained DL method and its applications.

Table 1
Composition of the alloys used in this work. Compositions are in weight percentages.

	Fe	C	Si	Mn	Ti	Nb	Cr	Ni
DP / DP-validation steel	Bal.	0.02	0.52	1.23	0.09	–	17.60	9.22
Q&P steel	Bal.	0.25	1.70	2.00	0.03	0.02	–	–
Q&P-validation steel	Bal.	0.27	1.64	2.22	0.01	0.01	0.01	–

site) and a Q&P steel (ferrite, martensite and RA), and the images were in different states, i.e., of lower qualities and taken at various magnifications, while high-quality SEM images of these two steels were used to train and test the DL model. The proposed EBSD-trained DL model was built based on U-net architecture using a small high-quality experimental dataset with EBSD ground truth. Once the DL models was well trained, it has three main applications: (1) classifying complex phases from SEM images; (2) skipping a lot of experimental effort to produce quasi-EBSD maps; and (3) high-throughput microstructure quantification combining the present model with the OpenCV package. The detailed implementation method is described below.

2.1. Dataset establishment

2.1.1. Experimental materials

In this work, microstructure of DP steel consists of austenite and martensite, which is produced by temperature-induced martensite transformation in austenite stainless steel. Such dual-phase microstructure is more complex than usual DP steel (ferrite and martensite [36]), representing a bigger challenge for accurate microstructural classification. The chemical composition of the DP steel, i.e., austenite stainless steel, used in this work is listed in Table 1. Ingot was prepared in the vacuum furnace. After forging, the material was heated to 1200 °C, held for 2 h, and then hot rolled into sheets of 3.5 mm. Subsequently, these sheets were solution-treated at 1050 °C for 5 h and then air cooled to room temperature. Through the above thermal processing, a metastable fully austenitic microstructure was obtained. Then, a sub-zero treatment was performed in liquid nitrogen to obtain a certain amount of martensite. The processing routine is shown in Fig. 2a. For the Q&P steel, the chemical composition is also listed in Table 1. The material was firstly hot rolled into sheets. Then, these sheets were annealed at 600 °C for 5 h and then air cooled to room temperature. After acid pickling, they were cold-rolled into sheets of approximately 1.2 mm thick. As shown in Fig. 2b, the sheets were reheated to the dual-phase region temperature of 790 °C, held for 80 s, and then cooled to 310 °C at a cooling rate of 30 °C/s and held for 50 s. Subsequently, they were reheated to 460 °C at a heating rate of 10 °C/s, held for 35 s, and then cooled to room temperature at a cooling rate of 30 °C/s.

2.1.2. Validation materials

In order to validate the general applicability of trained models, two validation steels were also prepared. For DP-validation steel, the composition of the steels remained the same, but a magnetic field instead of temperature was used to induce martensitic transitions. The experiment was carried out under magnetic field of 1 T in room temperature. For the Q&P-validation steel, a new alloy was selected with a composition also listed in Table 1. Also, the process parameters for the annealing and Q&P treatments were changed. The sheet was annealed at 650 °C for 5 h and then air cooled to room temperature. For Q&P treatment, the sheet was also reheated to the dual-phase region temperature at 790 °C, held for 60 s, and then air cooled to 240 °C and held for 40 s. Partition temperature and time were appropriate for this 2nd experimental steel grade.

2.1.3. Microstructure characterization

SEM and EBSD experiments were used to obverse the morphology and produce ground truth, respectively. For the SEM experiments, both backscatter electron (BSE) and second electron (SE) modes were applied to obverse the microstructures using a field-

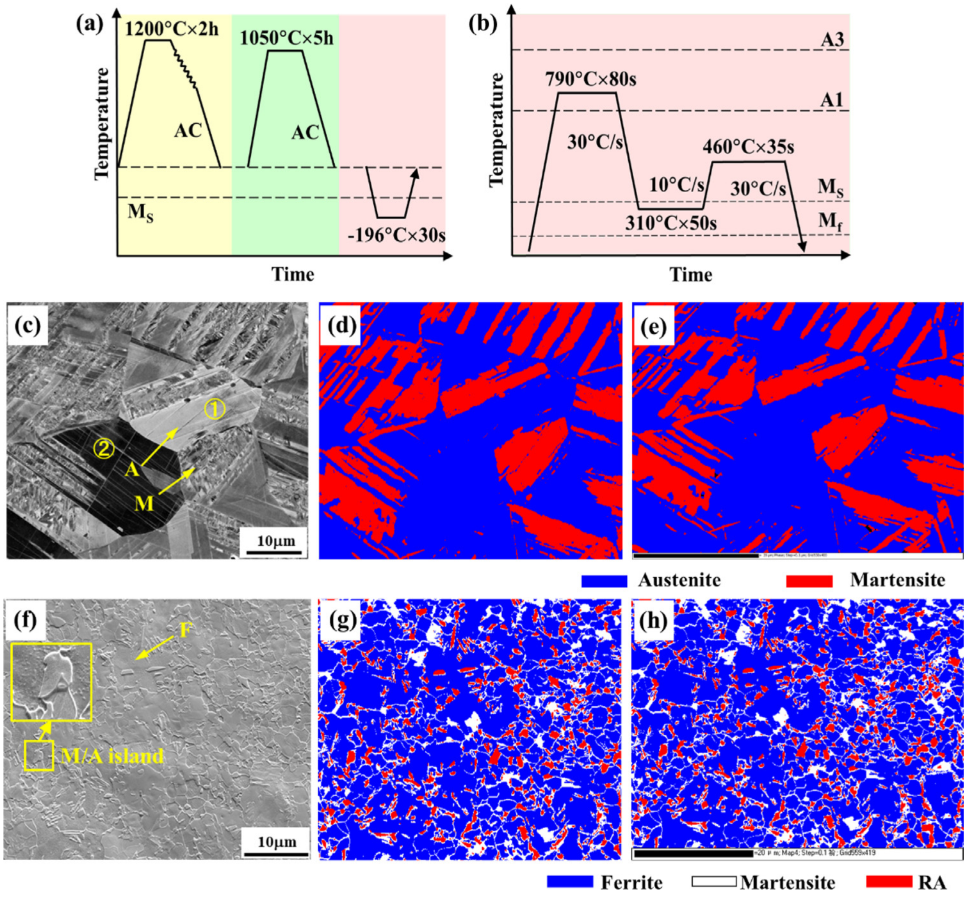

Fig. 2. The processing routes for the selected steels: (a) DP steel, (b) Q&P steel; the typical microstructures: (c) BSE image of DP steel, (f) SE images of Q&P steel; (d) EBSD ground truth from (c) BSE image; (g) EBSD ground truth from (f) SE image; (e, h) original EBSD maps.

emission scanning electron microscope (FE-SEM) system. The normal imaging rate (1000 ns/pixel) was used to produce high-quality images for building the training and testing dataset, and faster imaging rates, i.e., 100 ns/pixel, 200 ns/pixel and 500 ns/pixel, were used to acquire lower-quality images. EBSD experiments were conducted using a FE-SEM system with an accelerating voltage of 20 kV. A scanning step size of 0.1 μm was used to acquire ground truth datasets, and larger step sizes, i.e., 0.2 μm, 0.5 μm, 0.7 μm and 1.0 μm, were also used to investigate the experimental efficiency. The specimens were prepared by electrolytic polishing after mechanical polishing. The electropolishing solution was a mixture of 700 ml glacial acetic acid (CH3COOH) and 100 ml perchloric acid (HClO4). Electropolishing was conducted at 25 °C and 20 V for 20 s. In order to avoid the mechanically-induced martensite transformation of meta-austenite in Q&P steel during sample preparation, the grinding and polishing were carefully performed with very little force. As reported by Hofer et al. [41], a final manual polishing step should perform after electropolishing in order to prevent the transformation of the metastable retained austenite during preparation. However, this step is not available in present work because the surface morphology after electropolishing should be retained well for observing the SEM morphology to maintain the same morphology as in the EBSD experiment.

For the DP steel, BSE imaging was applied to characterize the microstructure, and these images were used as inputs of DL model. Then, the phase maps from EBSD experiment covering the same sample regions were used to accurately label the input BSE images based on the local crystal structure being martensite or austenite. In this experimental process, the BSE images were taken at predefined positions, and then the EBSD experiment was carried out at the same location over an area of approximately $56\mu m \times 44\mu$m at a magnification of 2000 × . The sizes of the collected standard BSE images were 1024 × 768 pixels. It is well known that the angle between beam direction and specimen is different for EBSD and BSE experiments, so a careful image registration is required between BSE image and its corresponding EBSD image. In this process, manual adjustment of the length and width of EBSD phase map was performed referred to corresponding BSE image to develop the good pixel correspondence between two images. Then regions with good pixel correspondence in SE and EBSD images were preserved to build dataset, and other redundant edge regions are cropped. For Q&P steel, secondary electronic (SE) imaging, instead of BSE, was used as this gives better morphological contrast. Electrolytically polished samples were used to observe the SE morphology to maintain the same morphology as in the EBSD experiment. The scanning area in the EBSD experiment was approximately $56\mu m \times 44\mu$m at a magnification of 2000 × and the pixel size of the SE image was 2048 × 1536 pixels. To classify the microstructures, the phase map of EBSD experiment was applied to distinguish fcc-structure RA and other bcc-structure phases. Ferrite and martensite were separated using a band scope (BS) map, in which martensite was defined by BS values of less than 90 and ferrite was defined by BS values greater than 90 [20]. For Q&P steel, SE mode was used to obverse morphology and SE image can be taken during EBSD experiment. Thus, a relatively good pixel correspondence exists between SE image and corresponding EBSD map due to the same angle between beam direction and specimen for SE and EBSD experiments, and only simple adjustments were required to reach precise pixel correspondence.

A typical BSE image of DP steel is shown in Fig. 2c, containing martensite (M) and austenite (A). It can be observed that most of the grain boundaries were somewhat fuzzy, and the morphological features of austenite in different locations were not consistent, such as location 1 and location 2 in Fig. 2c, representing a difficulty in the accurate classification. For the Q&P steel, which is a typical representative of 3rd generation advanced ultrahigh strength steels, proper microstructure segmentation is a longstanding issue, especially when classifying martensite and RA. A typical SE image of the Q&P steel is shown in Fig. 2f. The SE image contains two types of areas, in which the matrix phases are defined as polygonal ferrite presented as equiaxed, and other bulk-shape phases are regarded as “M/A islands” that include both martensite and RA. Although ferritic areas can be identified relatively easily by their morphology, determining exact locations of their grain boundaries is nontrivial. Moreover, martensite and RA mixed together show little differences in morphology and contrast, making it almost impossible to distinguish them just from the micrographs. But with the help of EBSD analysis, such complex microstructures can be clearly and faultlessly classified. The corresponding EBSD ground truth of Fig. 2(c and f) are shown in Fig. 2(d and g), respectively. The original EBSD phase maps are shown in Fig. 2(e and h).

2.1.4. Dataset construction

The DP steel dataset, named D_{DP}, contained 248 subimages (inputs) of 128 × 128 pixels cut from 6 original BSE images and 248 ground truth images from the phase maps produced by EBSD (outputs). For D_{DP}, the training set consisted of 208 subimages and the testing set was comprised of 40 subimages from one original BSE image. Only two phases (martensite and austenite) were present and classified as such to form the ground truth levels. The Q&P steel dataset, named D_{QP}, contained 726 subimages (inputs) of 128 × 128 pixels cut from 4 original SE images. The training set contained 656 subimages while the testing set contained 70 subimages cut from one original SE image. By combining the phase map and the BS map from the EBSD experiment, three-phase ground truth (outputs) were provided: ferrite + martensite + RA. These data are provided in the Supplementary Material. For the two datasets named above, common methods of data augmentation, e.g., flipping and random cropping, were used to expand the training data. After data augmentation, the number of training set increased to 1914 subimages for D_{DP} and 6048 subimages for D_{QP}. Moreover, common image processing methods, such as adjusting contract and brightness, were applied to balance the quality of the input images. For validation, one original BSE image consisting of 40 subimages from the DP-validation steel was used, and 70 subimages from an entire area of one original SE image of Q&P-validation steel was used. The corresponding EBSD phase maps were used as ground truth.

2.2. Modeling

2.2.1. Establishment of U-Net architecture

There are two reasons for the selection of U-Net architecture: first, it has shown an excellent performance in previous complex segmentation tasks with limited data in combination with data augmentation (e.g., biomedical images) [42,43]. Second, A unique “skip layer” is designed to connect the encoder and decoder, and is capable of avoiding the loss of detailed features during downsampling, which has the potential to maximize the guiding role of EBSD ground truth in model’s training. The structure of the model refers to the classical U-Net architecture reported by Ronneberger et al. [44], and consists of a contracting path and an expanding path. Four convention layers and four up-convention layers were located in contracting path and expanding path, respectively. The network architecture and some detailed information for each layer are illustrated in Fig. 3. The parameter padding was set as ‘same’ to maintain the feature map at the same size after the convolution operations. To prevent overfitting, batch normalization and dropout regularization with a rate of 50% were adopted [45,46]. The optimal parameter set for the U-Net architecture (including batch size, loss function and optimizer), was determined by trial and error. As mentioned in the previous section, two datasets, i.e., D_{DP} for DP steel and D_{QP} for Q&P steel, were built using experimental image data from two actual steels. Based on these datasets, two U-Net models with the highest segmentation accuracy were obtained via parameter adjustment, named DL_{DP}, DL_{QP} respectively. The optimal parameter sets of optimizer and loss function for above DL models are as follows: an AdaGrad optimizer [47] and a mean absolute error (MAE) loss function [48] for DL_{DP}, and an Adam optimizer [49] combined with MAE loss function for DL_{QP}. The batch size for above models is 32. Trained DL models can rapidly classify microstructures from input SEM images, and the quasi-EBSD maps can also be produced using available DL models, skipping the need for comprehensive and time-consuming physical EBSD experiments.

The U-Net architecture implementation was constructed using Python and the Keras framework. The training and testing were performed on a system equipped with an AMD® 2920X CPU @ 3.50 GHz (12 cores), 128 GB of RAM, and an NVIDIA GeForce RTX 2080Ti GPU with 11 GB of graphics memory.

2.2.2. Evaluation methods

This study used two standard evaluation metrics for semantic segmentation to evaluate the segmentation performance: pixel accuracy (*PA*) and mean intersection over union (*MIoU*). They are defined in Eqs. (1) and (2) [50], respectively:

$$PA = \frac{\sum_i n_{ii}}{\sum_i t_i} \tag{1}$$

$$MIoU = \frac{1}{n_{cl}} \sum_i \frac{n_{ii}}{t_i + \sum_j n_{ji} - n_{ii}} \tag{2}$$

where n_{ij} is the number of pixels of class i predicted to belong to class j; n_{cl} represents the number of different classes and $t_i = \sum_j n_{ij}$ is the total number of pixels of class i.

2.3. High-throughput quantitative metallography

Based on the present EBSD-trained DL model, an automatic quantitative method for microstructure analysis was applied using an image processing method based on the OpenCV package. The quantitative process was as follows. First, the target SEM images (SE or BSE modes) were cut into subimages of 128 × 128 pixels for use in segmenting the microstructures. For subimages with pixel size less than 128 × 128 pixels after cutting, resize function of OpenCV package can be used to convert them to standard size. Then, the microstructures in these subimages were classified based on the trained DL models, and the segmentation results for the original SEM images were obtained by splicing all the subimages. Finally, the quantitative microstructural data were calculated according to the statistics of the pixel information obtained for each phase.

3. Results

3.1. Experimental materials

3.1.1. Segmentation result of DP steel

The segmentation results of DP steel by DL_{DP} model are shown in Fig. 4. Fig. 4a shows the statistical distribution of the two evaluation indexes *PA* and *MIoU* of testing set, in which six numerical

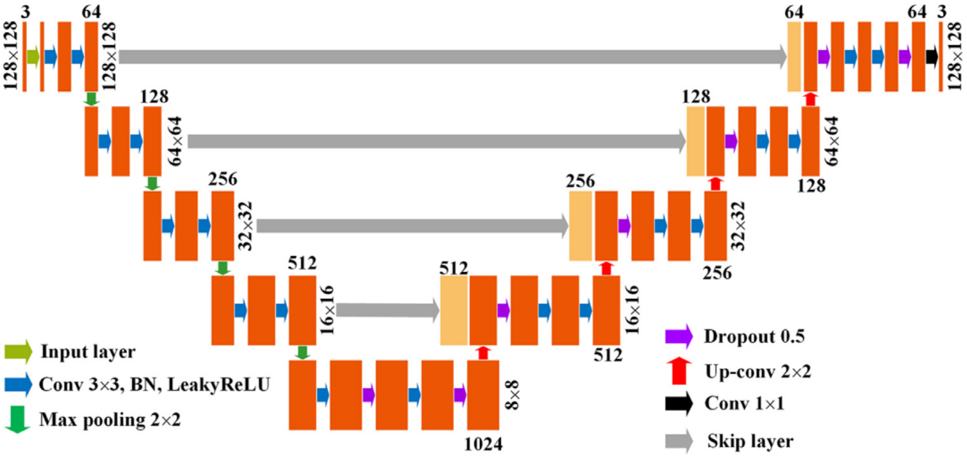

Fig. 3. The U-Net network architecture. The numbers on the top (or bottom) and at the right (or left) of each block correspond to the number of filters and the size of the feature map, respectively.

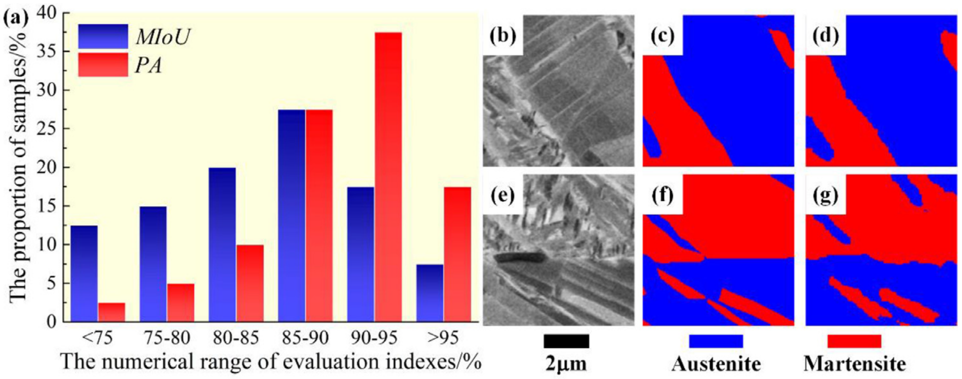

Fig. 4. The segmentation results of DP steel: (a) the distribution of the evaluation indices *PA* and *MIoU*; (b, e) BSE images of two areas taken from the testing images, (c, f) corresponding EBSD ground truth and (d, g) corresponding segmentation results.

value ranges for the evaluation indexes are plotted along X-axis and the proportion of the number of samples in each numerical range to the total is plotted in Y-axis. The *PA* is the pixel accuracy, and *MIoU* represents the ratio of the intersection and union of the segmentation result and ground truth of each class. The *PA* values are mainly distributed in the range above 85% with a mean value of 90.1% (±5.8%), showing the good pixel consistency between segmentation result and ground truth. The *MIoU* values are mainly concentrated in the range of 80%–95% with a mean value of 83.2% (±9.3%), indicating a good segmentation accuracy. Fig. 4b-g shows two cases taken from the testing set: the BSE image (b, e), the ground truth (c, f) and the segmentation results (d, g). As shown in Fig. 4(b and e), these BSE images contain ambiguous grain boundaries and fine and non-easily identifiable features between the martensite and austenite, which would be hard to classify accurately by human microscopists leading to datasets with incorrect ground truth values. Any incorrect classification automatically lowers the accuracy of the DL models trained on these data. However, such BSE images can be accurately calibrated using phase maps from the EBSD experiment, as shown in Fig. 4(c and f). Thus, with the assistance from the EBSD, the proposed method achieved accurate classification results compared with the true labels as shown in Fig. 4(d and g).

3.1.2. Quantitative analysis of DP steel

In present work, an automatic quantitative image analysis method is proposed by combining the EBSD-trained DL model and the OpenCV package. One original BSE image (cut into 40 128 × 128-pixel subimages) of DP steel taken at 2000 × magnification was used to determine the martensite content. The selected BSE image from testing set is shown in Fig. 5a. The recording of this area on the SEM took only 25 s. The related microstructure classification result using DL_{DP} model is shown in Fig. 5b, where martensite and austenite are marked in red and blue. The complete quantitative process of present DL-based method, including the previous segmentation process, takes only approximately 35 s, indicating its high efficiency. In contrast an actual EBSD experiment for the same image takes approximately 100 min with a scanning step size of 0.1 μm to produce the phase map as shown in Fig. 5c. In addition, the quantitative results of the phase map of EBSD analysis can be used as reference to evaluate the accuracy of the present DL-based quantitative method, which is more reliable than referring to manual ground truth[51]. To better quality the results, the deviation is used to describe quantitative error between present method and EBSD, and its value is the absolute value of the quantitative result of present method minus EBSD quantitative result. The distribution of these deviations of 40 subimages between EBSD and the present method is plotted in Fig. 5d. It is observed that the majority of deviations were less than 6%, showing the good accuracy and stability of this automatic quantitative method. Moreover, the scanning area of each subimage is very small, only approximately 50 μm^2, also indicating the strong ability to analyze the microregions. With respect to the whole image, the quantitative results of the two methods also demonstrated a high consistency, i.e., 38.5% for the present method and 35.2% for the EBSD analysis, also showing the applicability to regular SEM

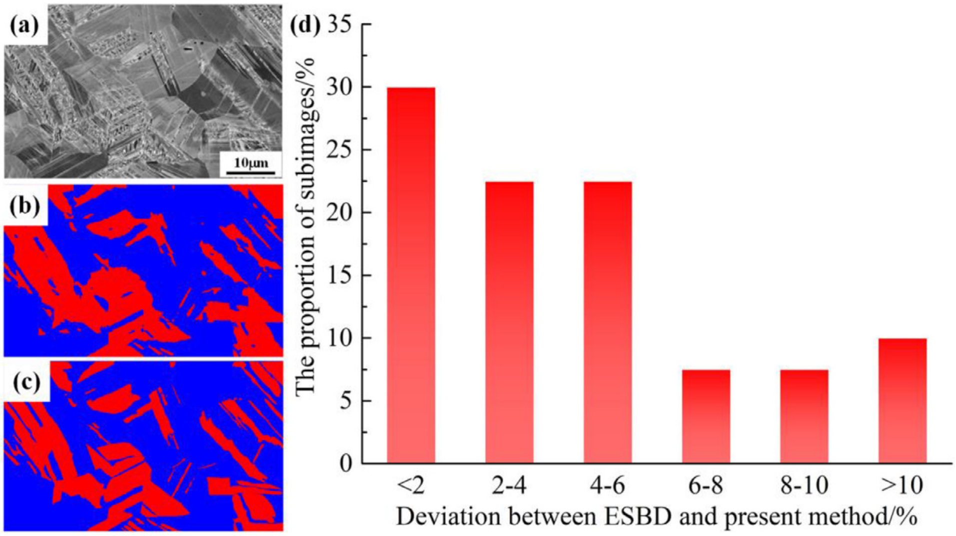

Fig. 5. Quantitative analysis of martensite content in DP steel: (a) original BSE image, (b) segmentation result and (c) ground truth for calculating martensite content; (d) distribution of deviations of quantitative results between EBSD and the present method.

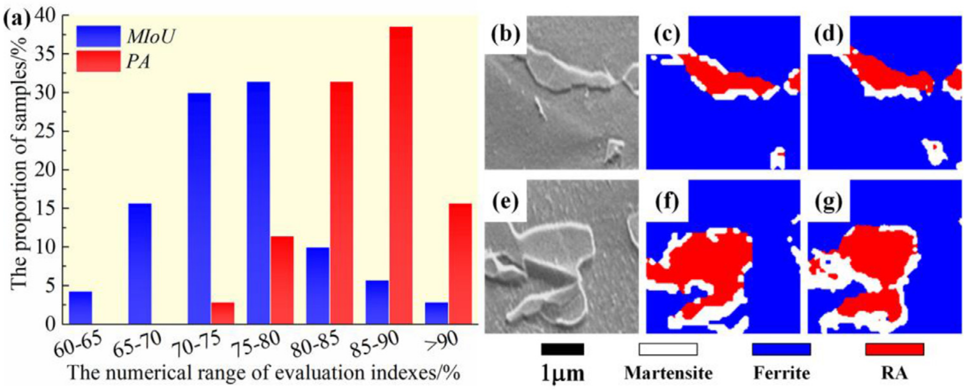

Fig. 6. The segmentation results of Q&P steel: (a) the distribution of the evaluation indices *PA* and *MIoU*; (b, e) SE images of two areas taken from the testing images, (c, f) corresponding EBSD ground truth and (d, g) corresponding segmentation results.

images covering a large scanning area (in this case: about 2000 μm^2).

3.1.3. Segmentation results of Q&P steel

The distribution of the two segmentation evaluation indexes of testing set is plotted in Fig. 6a. For *MIoU*, the mean value of all samples in testing set is 75.5% (±6.5%), and the majority of values is concentrated in the range from 70% to 80%, which accounts for 61.4% of the total. With respect to *PA*, about 86% of the results are located in the range from 80% to 100% with the mean value of 85.4% (±5.1%). Two cases from the testing set, containing SE images (b, e), ground truth (c, f) and segmentation results (d, g) are shown in Fig. 6b-g. Although no fine features in morphology and contrast can be observed in each M/A island in the BSE images in Fig. 6(b and e), the EBSD-trained DL_{QP} model has the ability to classify not only the ferrite matrix and the M/A island, but also the actual distribution of martensite and RA inside each M/A island based on the accurate ground truth as shown in Fig. 6(c and f). These segmentation results as shown in Fig. 6(d and g) are basically consistent with the ground truth.

3.1.4. Quantitative analysis of Q&P steel

For the Q&P steel, an original SE test image (later cut into 70 128 × 128-pixel subimages) shown in Fig. 7a is used for the quantitative image analysis. The image was first segmented into ferrite, martensite and RA, respectively, using DL_{QP} model. The EBSD ground truth and segmentation result are shown in Fig. 7(b and c), in which ferrite, martensite and RA are presented in blue, white and red, respectively. Compared to the EBSD ground truth, shown in Fig. 7b, the microstructure in the SE image (Fig. 7a) was could be reconstructed with good accuracy into martensite, ferrite and RA as shown in Fig. 7c. Fig. 7(d and e) give the detailed quantitative results of the EBSD analysis and the present method, respectively. With respect to phase content as shown in Fig. 7d, it can be seen that the quantitative results of the present method are in good agreement with EBSD analysis, and the deviation value of each phase is within 1.0%. Particularly for RA, the deviation value is only 0.1%. The area of RA reconstructed using the segmentation result and that obtained via EBSD is shown in Fig. 7e. Although the present method slightly underestimates the RA area, such as the frequency of DL method is lower than EBSD for RA with the area >1.0 μm^2 (frequency: 1.7% for DL method, 7.0% for EBSD), the frequency in other area ranges was highly consistent between both methods.

3.2. Results obtained on the two validation steels

The morphology of the DP-validation steel is shown in Fig. 8a. Compared to the microstructure of the DP steel used for training and testing dataset (shown in Fig. 5a), it the martensite content in

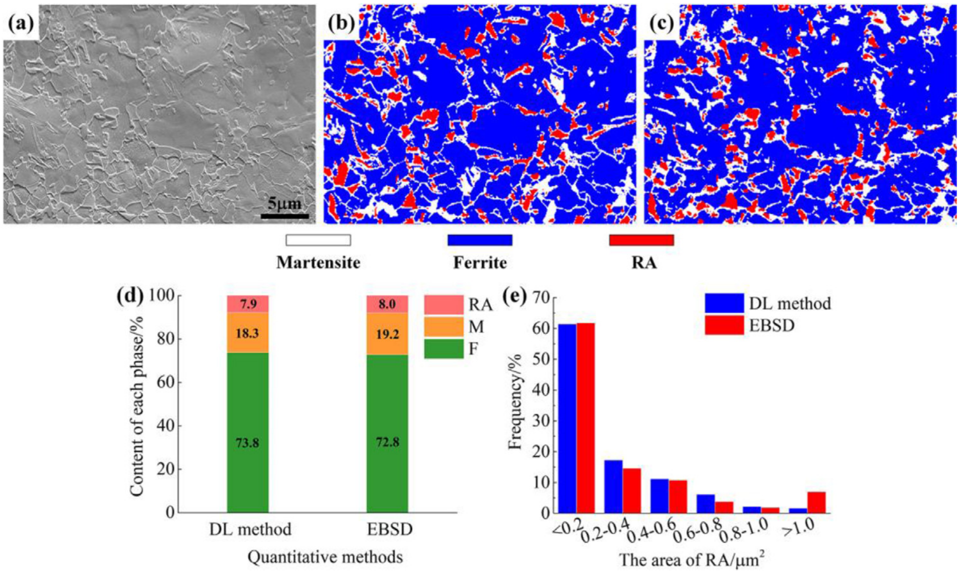

Fig. 7. The quantitative analysis of Q&P steel. (a) the SE image, (b) EBSD ground truth and (c) segmentation result; (d) phase content calculated based on present method and EBSD; (e) the distribution of area of RA from present method and EBSD.

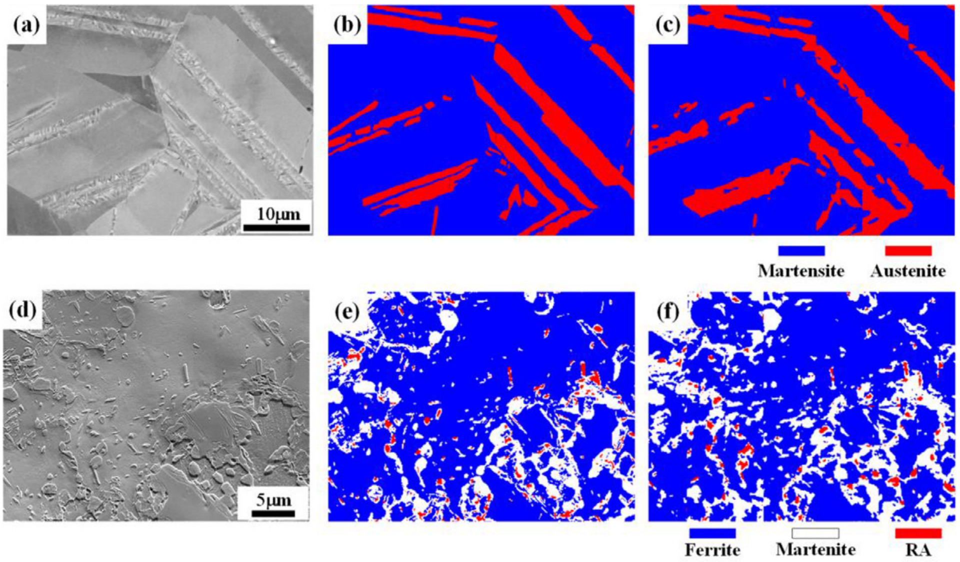

Fig. 8. Segmentation and quantitative analysis of validation steels: (a) BSE image, (b) EBSD phase map and (c) segmentation result of DP-validation steel; (d) SE image, (e) EBSD result and (f) segmentation result of Q&P-validation steel.

the validation steel is significantly lower and the martensite basically exists in the form of laths. Given the EBSD phase map shown in Fig. 8b, it is clear that the $\mathrm{DL}_{\mathrm{DP}}$ model trained on the other DP steel is found to be surprisingly capable of accurately identifying martensite and austenite of this validation steel as shown in Fig. 8c. The martensite content for the segmentation image is 19.8%, which is very consistent with the EBSD result, i.e., 19.1%.

The microstructure of the Q&P-validation steel is shown in Fig. 8d. It consists of a coarse-grained ferrite matrix and many small M/A islands, which are completely different in appearance from those observed in the original training and testing sets as shown in Fig. 7a. Again, the martensite and RA inside M/A islands do not show obvious differences in morphology or contrast. The segmentation result of trained $\mathrm{DL}_{\mathrm{QP}}$ model is shown in Fig. 8f. It is found that not only ferrite matrix and M/A islands are properly identified, but also the martensite and RA phases inside M/A island are identified with acceptable accuracy as shown in Fig. 8e. Based on the segmentation results, SE image (Fig. 8d) contains 71.1% ferrite, 26.9% martensite and 2.0% RA, which is in good agreement with the EBSD result, i.e., 74.6% ferrite, 23.3% martensite and 2.1% RA. The above segmentation and quantitative results for the validation steels strongly proves the good applicability of present method for microstructure segmentation and quantification for different kinds of steels. It also shows that a well-trained model can be used to properly analyze other (related) steels for which it was not trained.

4. Discussion

4.1. The complexity of segmented microstructure

In previous studies [36,37], DL-based microstructural analysis was applied only to simple and relatively coarse microstructures having clearly distinctive morphologies and easily locatable phase boundaries. In such cases human phase identification to form a reliable training set can work well, but DL becomes significantly less powerful if the training data is corrupted by incorrect data. EBSD can provide significantly more accurate labels for complex and fine microstructures, which enables DL-based methods to be expanded to fine and complex microstructures. Once the model is established and trained, quasi-EBSD maps can be obtained by inputting simple SEM results, without time-consuming and costly EBSD experiments yet keeping an accurate estimate of the real microstructure.

As far as DP steels are concerned, in most cases, its microstructure is composed of martensite and ferrite [52,53]. Such phases can be clearly identified on the basis of their SEM morphology and hence they have been properly classified based on the DL method [36]. In the present work, the selected DP steel contains austenite and martensite as shown in Fig. 4(b and e), which are more difficult to be classified because of their fuzzy SEM morphology. But an EBSD-trained DL-based method is capable of segmenting the images properly as shown in Fig. 4(d and g) and it quantified the microstructures with a very high accuracy. The QP steel studied here contained three types of phases (see Fig. 6(b and e)), i.e., ferrite, martensite and RA, but only two types of phases, i.e., ferrite and M/A islands, can be distinguished based on just their SEM morphology. That implies that traditional DL models without EBSD information and manual calibration can only provide two-phase ground truth data. However, the EBSD data showed clearly that the M/A islands in Q&P steel consisted of martensite and RA, which are almost completely indistinguishable in the SEM images due to minimal morphological contrast and invisible phase boundaries. In the present work, the complex microstructure was classified using EBSD analysis to solve the labeling problems as shown in Fig. 6(c and f). Then, the smart DL model was applied to discover the correlation between the phase species and their comprehensive morphologies because it has a strong ability to extract image features by sensing the small differences in the contrast, grayscale, etc., based on computer vision, and finally these complex microstructures were successfully classified, as shown in Fig. 6(d and g). While the EBSD trained model using high resolution imaging clearly showed positive results, it is interesting to examine its behavior under less-optimal imaging conditions and to examine why the method as developed performs so well.

4.2. Robustness to low-quality images

In earlier DL-based microstructure segmentation attempts the datasets used for training and evaluation consisted only of images of equal high quality [35–38]. However, when evaluating many samples or evaluation samples over an extended period of time the stability of the quality of the SEM images cannot be guaranteed. Furthermore, sometimes low-quality images may be taken intentionally to speed up data gathering and to reduce the costs involved in microstructure classification. To study the robustness of the classification model developed in the basis of a high-quality images, new lower resolution BSE images of the DP steel were collected using three faster imaging rates (i.e., 100 ns/pixel, 200 ns/pixel and 500 ns/pixel). In addition, BSE images with a normal imaging rate (i.e., 1000 ns/pixel), were also obtained from the same area as the reference. To make the robustness test even more critical, the experiments were conducted on another FE-SEM with a longer service life. EBSD experiments were conducted to produce the ground truth for the BSE image, and 20 subimages of 128 × 128 pixels from each original BSE images with the different imaging rate were used to test the robustness of $\mathrm{DL_{DP}}$ model to low-quality images. To compare the differences between the normal and low-quality images, their grayscale distributions were calculated using OpenCV and they are shown in Fig. 9a. Significant grayscale differences exist between the various BSE images. The gray values for the high-resolution images are distributed over a wide range from 50 to 200. The gray values of the three low-quality BSE images are distributed over a much smaller range, spanning values from 75 to 150. The change in segmentation results of BSE images with different qualities is shown in Fig. 9b. Although the segmentation accuracy decreases with decreasing image quality, the mean values of *MIoU* and *PA* of 20 subimages are still greater than 71.7% and 81.3%, respectively, even for BSE images with an exposure rate of 100 ns/pixel. as shown in Fig. 9c and 9d, respectively. Under these conditions the input image had a poor contrast between the two phases and, in comparison to the reference image shown in Fig. 9i, included massive amounts of noise. However, martensite and austenite could still be properly segmented using the $\mathrm{DL_{DP}}$ model trained on high-quality input images. As the imaging rate increased to 200 ns/pixel, the segmentation accuracy increased and the mean values of *MIoU* and *PA* reach 76.2% and 85.0%, respectively, as shown in Fig. 9f. For the BSE image with an exposure rate of 500 ns/pixel, the mean values of *MIoU* and *PA* increase to 82.5% and 89.1%, respectively, and a high segmentation accuracy is obtained, which is quite close to that of the $\mathrm{DL_{DP}}$ model when applied to the high-quality images (82.9% for *MIoU* and 90.1% for *PA* respectively). The above segmentation results demonstrated that the present DL model trained by high-quality image data is capable of being directly expanded to low-quality images with massive noise and experimental instruments with different capacities. The reason for this robustness will be explained in more detail in Section 4.5.

4.3. Robustness to images taken at different magnifications

In the metallographic practice pictures are often taken at different magnifications to either get a more general overview or to record fine details. In this study, the $\mathrm{DL_{DP}}$ model trained via input images at a magnification of 2000 × was used to examine its ability to analyze images taken at different magnifications. The results for the images taken at 2000 × and reported in Section 3.1, ((83.2% (±9.3%) for *MIoU* and 90.1% (±5.8%) for *PA*) were used to set the reference level. Images taken at magnifications of 500 ×, 1000 × and 4000 × are shown in Fig. 10a-c. At magnifications of 500 × and 1000 ×, the morphology of the microstructures remained close to that in the reference images. When the magnification was increased to 4000 ×, new and more detailed features of martensite laths were observed and the overall morphology differed from the reference morphology. The segmentation accuracy of the model as a function of the magnification is shown in Fig. 10d. As shown in Fig. 10d, the segmentation results of images taken at different magnifications do not deviate significantly from the reference level, and all the deviation values are below 3%. These results demonstrate that the current U-Net model shows high generalizability for images with various magnifications. Two examples for the BSE images at magnifications of 500 × and 4000 × are shown in Fig. 10e-g and h-j, respectively, showing that the segmentation results are in good agreement with the ground truth. Although changes in magnification do slightly affect the stability of the proposed method, the model still obtains good segmentation results.

4.4. Comparison of the present DL-based method and the traditional binary method

Traditionally, to obtain the phase fraction results directly from OM or SEM images, the images are converted into binary images using image processing, and then the quantitative results are obtained based on an experimentally determined threshold value. In order to demonstrate the advantages of the automatic quantitative method used in the present work, the traditional binary method was also used to perform microstructure quantification of the DP steel. A selected area of 384 × 384 pixels is shown in Fig. 11a.

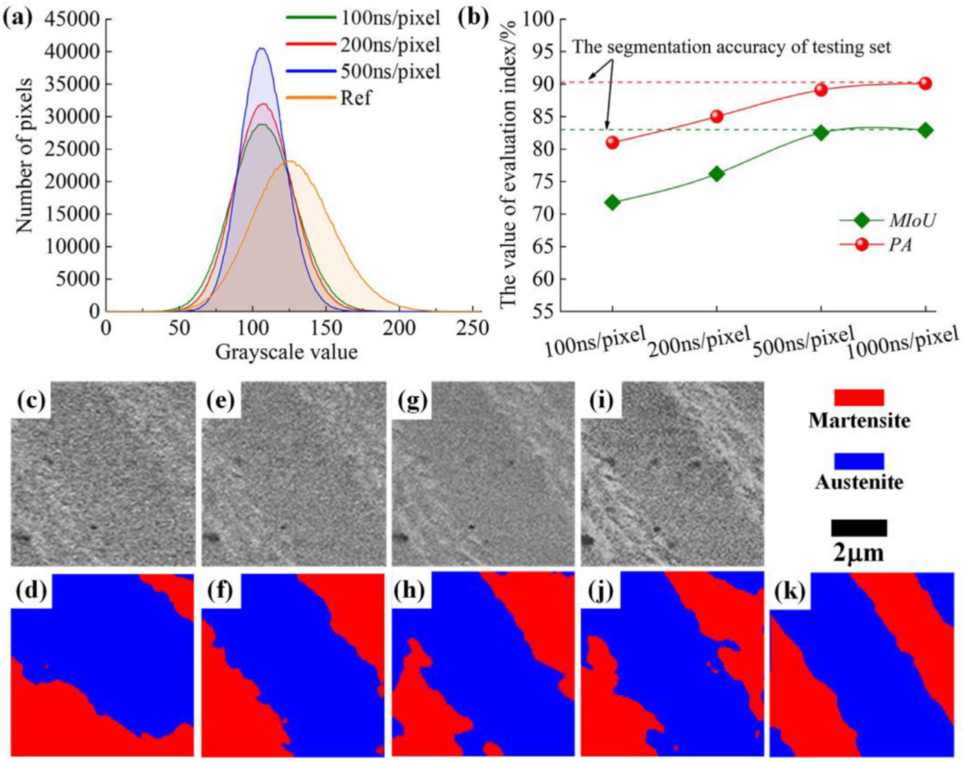

Fig. 9. (a) The grayscale distribution of BSE images with various qualities; (b) the segmentation results of BSE images with various qualities by the DL_{DP} model trained on high-quality images; the detailed cases of images with various qualities and ground truth: (c) BSE image and (d) segmentation result for an imaging rate of 100 ns/pixel; (e) BSE image and (f) segmentation result for an imaging rate of 200 ns/pixel; (g) BSE image and (h) segmentation result for an imaging rate of 500 ns/pixel; (i) BSE image and (j) segmentation result for an imaging rate of 1000 ns/pixel; (k) ground truth.

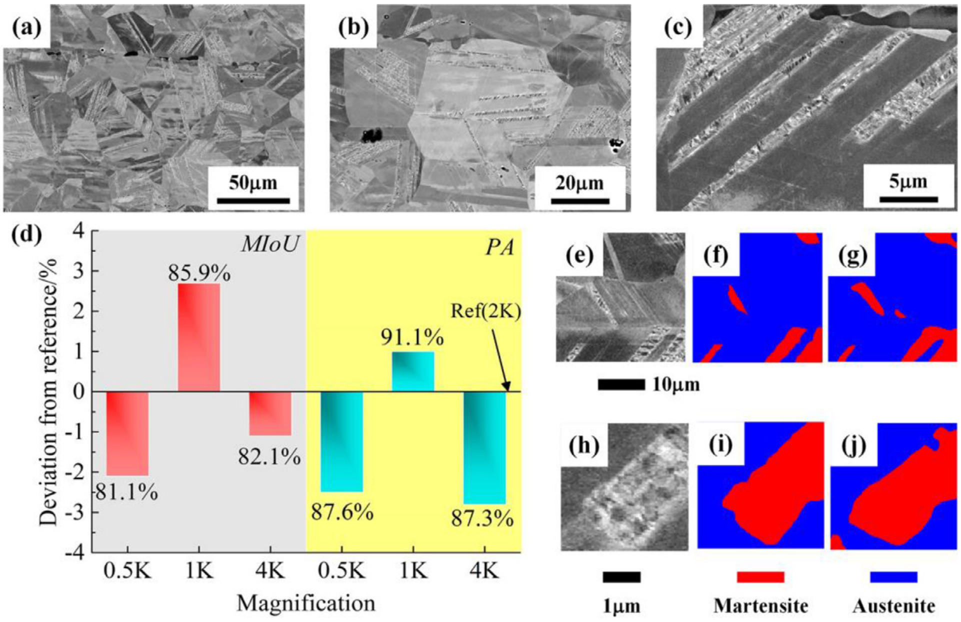

Fig. 10. The SE images at the magnification of (a) 500 ×, (b) 1000 × and (c) 4000 ×; (d) the deviations of evaluation indexes between images with magnifications of 500 ×, 1000 × and 4000 × and the reference image with 2000 × magnification; two segmentation cases for the BSE images at the magnification of (e-g) 500 × and (h-j) 4000 ×: (f, i) EBSD ground truth, (g, j) segmentation results.

Based on the phase map of EBSD analysis shown in Fig. 11b, the reference value of the martensite content is 16.6%. Using the new DL-based quantitative method, the martensite content was evaluated as 17.5%, as shown in Fig. 11c—a result that is basically consistent with the result of EBSD analysis. In the binary images, the martensite content was calculated by counting the portion of white pixels among the total pixels, where martensite and austenite are represented by white and black, respectively. To study the effect of the threshold value on the quantitative result, threshold values ranging from 130 to 155 were chosen to calculate the apparent martensite content. Fig. 11e shows that the martensite content changes almost linearly with the threshold value. Varying the

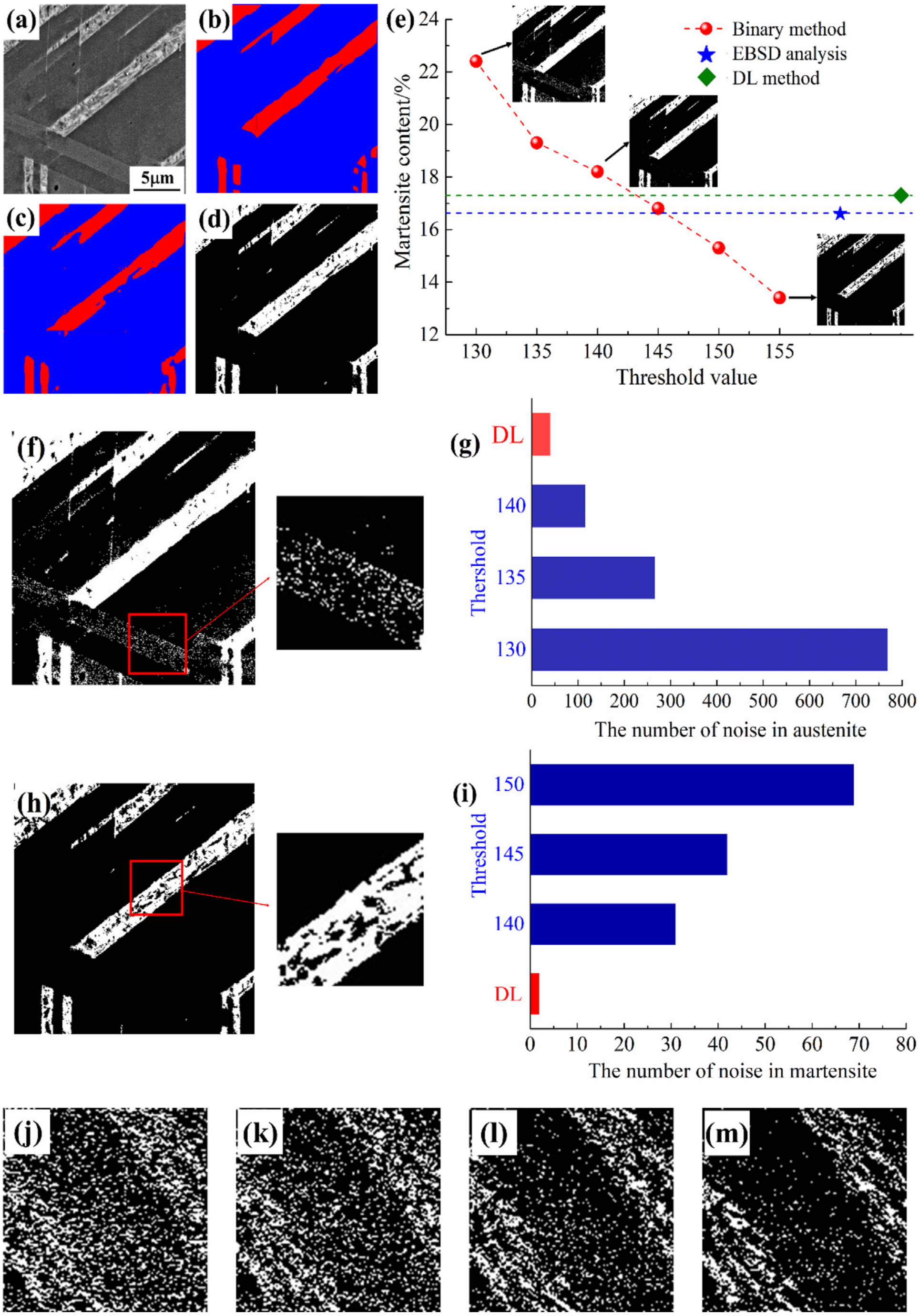

Fig. 11. Comparison between the proposed method and a traditional binary image method: (a) BSE image; (b) EBSD phase map; (c) segmentation result; (d) result of binary image; (e) variation in measured martensite content as the threshold value changes. (f) The binary image with noise in austenite; (g) comparative result for the number of noises in austenite between the binary method and the present method; (h) the binary image with noise in martensite; (i) comparative result for the number of noises in martensite between the binary method and the present method; Segmentation result of low-quality images using binary method: (j) the imaging rate of 100 ns/pixel; (k) the imaging rate of 200 ns/pixel; (l) the imaging rate of 500 ns/pixel; (m) the imaging rate of 1000 ns/pixel.

threshold from 130 to 150 changed the martensite are fraction from 22.4 to 13.4%, However, while the fraction levels changed significantly the morphologies as represented in the binary images remained remarkably similar. In addition to the phase fraction, the grain size is also an important piece of microstructural information. In the binary method, this is not so simple to determine. As shown in Fig. 11f (threshold value of 130), when a relatively low threshold is selected, martensite being the white phase is segmented well. However, many white "martensite" with a small size exist in the austenite as the black phase. From metallographic experience we know, these "white phases" are the noise, not actual martensite. The number of noises in austenite in the binary images with different threshold values and the DL segmentation results are shown in Fig. 11g. Although the amount of noise continuously decreases with the increase of the threshold value, the amount of noise in the binary image with the threshold value of 140 is still an order of magnitude higher than that of the DL result. As the threshold value continues to increase, the noise in austenite nearly disappears, but the black noise as "austenite" starts to appear in the martensite lathes, as shown in Fig. 11h. The number of noise

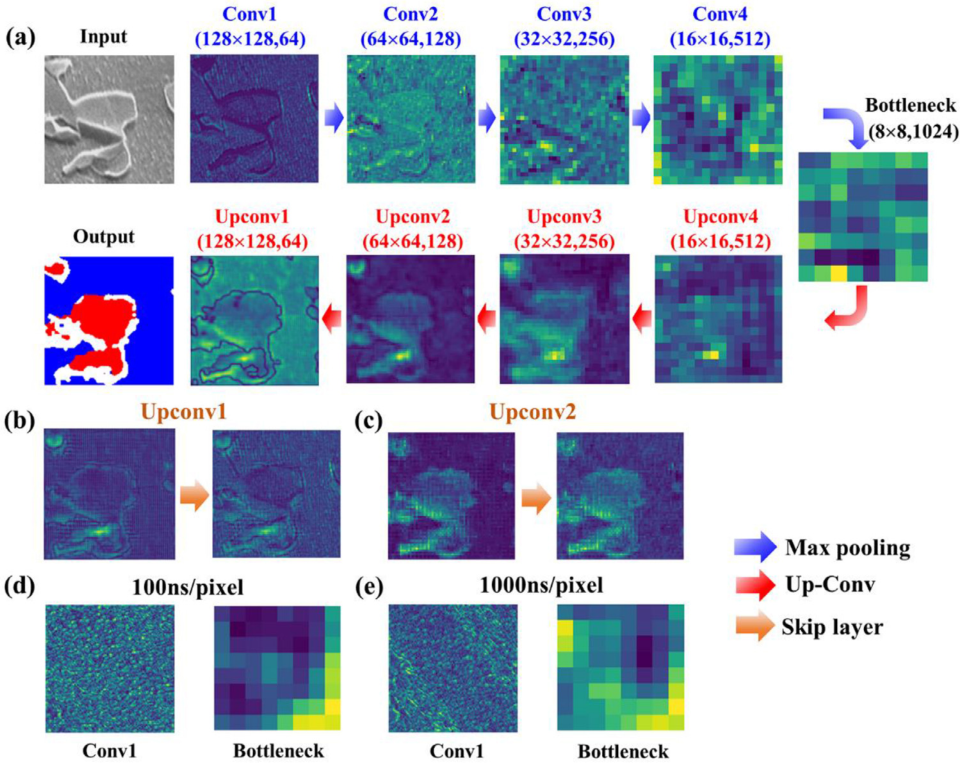

Fig. 12. (a) Visualization of feature maps in the U-Net architecture, a case for Q&P steel; the original feature map and the enhanced feature map from the "skip layer" in (b) Upconv1 and (c) Upconv2; feature maps of Conv1 and Bottleneck for input images with imaging rates of (d) 100 ns/pixel and (e) 1000 ns/pixel, respectively.

pixels in martensite in the binary images with different threshold values and the DL segmentation result is shown in Fig. 11i, showing that the amount of noises in the binary method is much higher than that in the DL result. The segmentation results of low-quality images (as shown in Fig. 9c, 9e, 9 g and 9i) using the binary method are shown in Fig. 11(j-m). It can be clearly seen that the binary method lacks the ability to accurately classify ferrite and martensite due to the small pixel difference between two phases and amounts of noise, showing the high sensitivity of classification accuracy to image quality. However, DL-based method is capable of reliably segmenting microstructures as shown in Fig. 9, demonstrating that present DL-based method has a stronger robustness and practical application ability than traditional binary method.

4.5. The origin of the model's good performance

To better understand the origin of the excellent performance and stability of the present model based on the U-Net architecture, the entire segmentation process is visualized using feature maps [54,55], as shown in Fig. 12a, where feature extraction was conducted through the convolution operations (i.e., Conv1–4), while the output construction process was conducted via up-convolution, i.e., Upconv1–4 (see Fig. 3). The brightness in Fig. 12a indicates the feature strength at a given location in the feature map, in other words, the brightness of a location directly represents its level of importance for segmentation. Clearly, the ferrite and M/A islands in the input image can be distinguished well via the Conv1 and Conv2 feature maps according to the extracted morphology using trained filters, and brightness differences can be observed inside the M/A islands, indicating that different phases may exist there. These differences provide a good basis for classifying ferrite, martensite and RA in SE images. Although the feature maps in Conv4 and bottleneck layer may seem difficult to understand, apparently, the important features are extracted and stored in these maps. In the subsequent up-convolution process, the detailed features of input image are recovered. Note that after two up-convolutions, the morphology of the input image has basically been recovered in Upconv2. Moreover, the detailed information is continuously enriched in the subsequent process. The final output is similar to the ground truth from the EBSD experiments. In conclusion, the good generalizability of the present model stems from the suitable complexity of the designed U-Net architecture, which is capable of fully mining the dataset information. On the other hand, the reliable ground truth from the EBSD analysis is also fundamental to achieving the accurate results because it provides the correct "knowledge" from which the DL model learns.

The present U-Net architecture differs from other segmentation networks in that it adopts a unique "skip layer" that directly transfers the convolution layer feature maps to the corresponding up-convolution layers, ensuring that the detailed information is not lost in the total segmentation process. In order to clearly show this role, two feature maps before and after "skip layer" in Upconv1–2 layers are shown in Fig. 12(b and c). The feature maps processing via "skip layers" have better resolution compared to the original feature maps due to the enhancement of the detail information. The existence of such "skip layer" not only enables EBSD ground truth to be used for training network parameters, but also enables the morphological information extracted in contracting path to be used for again output construction in expansive path, which greatly enhances guidance role of EBSD labels on model training. Moreover, visualizing the feature maps is also a good approach for explaining why the model is robust to low-quality images with massive amounts of noise. Fig. 12 (d and e) show the feature maps of Conv1 and bottleneck layer from the images with imaging rate of 100 ns/pixel and 1000 ns/pixel, respectively for which the input images have been shown in Fig. 9(c and i). With respect to Conv1, the greatest difference still exists in feature maps between images with 100 ns/pixel and 1000 ns/pixel because of the difference in

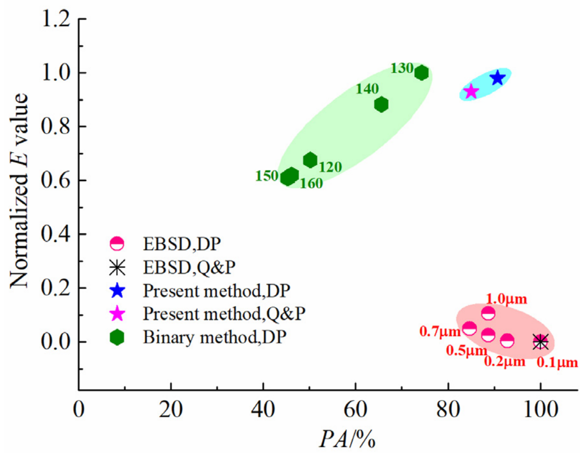

Fig. 13. Comparison of computational efficiency and classification accuracy among present method, EBSD and binary method. The number marked on points represents the step size in EBSD region and threshold value in the region of binary method, respectively.

morphology. However, for the bottleneck layer, the feature maps of two images are very similar and the areas with high brightness are located in the bottom right corner, indicating that accurate and important features are successfully extracted from the low-quality images by the accurate DL model trained via EBSD-trained ground truth even when faced with large noise effects. Thus, this model provides a good basis for constructing reliable output.

4.6. Computational efficiency

In the present work, the computational efficiency E is defined by equation: $E = {}^{PA_i}/_{t_i}$, in which PA_i and t_i represent the pixel accuracy and time of obtaining the phase map of SEM image i, respectively. In a DL-based method the computational time mainly depends on the network size [56] (e.g., the number of layers). The present U-Net model takes only about 10 s to process a standard SEM image using the relatively simple network structure as shown in Fig. 3, the *PA* values, as described in Sections 3.1.1 and 3.1.3, were used to calculated to E value. For EBSD, various scanning steps were used to produce phase maps with different experimental time, i.e., 0.1 μm, 0.2 μm, 0.5 μm, 0.7 μm and 1.0 μm. The phase map with 0.1μm was used as ground truth (*PA* value: 100%) to calculate the *PA* values of phase maps with other step size. For binary method, the experimental time was about 8 s for processing a SEM image. The thresholds were adjusted to produce different segmented results, and the *PA* values of each segmented results were calculated refer to corresponding EBSD phase map. Based on above experimental time and *PA* value, the E values of each method were calculated. According to normalized E value and *PA* value, each method is plotted in E-*PA* space in Fig. 13. For binary method, some points had a relatively high computational efficiency with the E value from 0.6 to 1.0, but a relatively low *PA* values, representing its limited ability for microstructure classification. Moreover, the binary method can only be applied to identify simple microstructures of dual-phase materials based on the contrast, and cannot be applied to complex multi-phase microstructures, such as Q&P steel. For EBSD, all points are located in the right-bottom corner, which shows that it has a unique superiority in classification accuracy but the time cost is also very high. It can be seen that the E and *PA* values of present DL-based method are concentrated in the region of high E (0.93–0.98) and *PA* (85%−91%), indicating its high accuracy and computational efficiency. DP steel obtains larger E value than Q&P steel because it has the higher *PA* value. Although dataset construction and model training require a certain amount of time, the trained DL model is capable of rapidly producing an EBSD map using only regular SEM images. Compared to binary method, present DL method has similar efficiency but a much higher segmentation accuracy. Compared to EBSD, the present DL method has a much higher efficiency in combination with an almost equal accuracy.

5. Conclusion

A novel method for complex microstructure segmentation and quantification of engineering steels requiring only small experimental data sets is presented, which expands the DL method to extremely complex microstructures by integrating EBSD labeling and DL. The present method showed significant advantages in accuracy, generality, robustness and efficiency over previous DL methods:

(1) The present method was successfully applied to DP and Q&P steels. It is not only able to analyze DP steel (M-A) with ambiguous grain boundaries, but also to accurately quantify microstructure of Q&P steel, especially martensite and RA inside M/A island, which indicates that the EBSD-trained DL method possesses good generality by eliminating the limits of labeling error incurred by manual experience in the conventional DL method.
(2) The present method achieved a success application of validation steels of DP and Q&P steels, and the quantitative results were in good agreement with EBSD experiments, showing that the trained model also could be used to adequately analyze other (related) steel for which it was not trained.
(3) The present method could be applied successfully for the two modes of SEM imaging, i.e., SE and BSE, with different qualities (imaging rate: 100~1000 ns/pixel) and different magnifications (500~4000 ×), indicating its impressive robustness and good application prospect in practical scenarios.
(4) The present method showed advantages in both accuracy and efficiency. It has better accuracy than traditional binary method and higher efficiency than EBSD experimental method. Moreover, EBSD phase maps can be rapidly produced only using regular SEM images via trained models, skipping time-consuming experiments and contributing to accelerate EBSD analysis.
(5) The accurate EBSD ground truth provided an essential foundation for good performance, and the “skip layer” of U-Net model enhanced the guiding role of EBSD analysis. This combination provided a bright prospect for hybrid DL methods and physical metallurgy for high-throughput quantitative metallography in order to accelerate material development.

Declaration of Competing Interest

The authors declare that they have no known competing financial interests or personal relationships that could have appeared to influence the work reported in this paper.

Acknowledgments

This work was financially supported by the National Natural Science Foundation of China (Grants No. 51722101 and U1808208). The authors also gratefully acknowledge the financial support provided by the National Key R&D Program (Grant No. 2017YFB0703001) and major scientific and technological innovation projects of Shandong Province (Grant No. 2019TSLH0103).

Supplementary materials

Supplementary material associated with this article can be found, in the online version, at doi:10.1016/j.jmst.2021.04.009.

References

[1] P. Gao, M. Fu, M. Zhan, Z. Lei, Y. Li, J. Mater. Sci. Technol. 39 (2020) 56–73.
[2] E.C.H.C. O' Brien, H.K. Yeddu, J. Mater. Sci. Technol. 49 (2020) 157–165.
[3] D.P. Yang, P.J. Du, D. Wu, H.L. Yi, J. Mater. Sci. Technol. 75 (2021) 205–215.
[4] T. Chen, L. He, M.H. Cullison, C. Hay, J. Burns, Y. Wu, L. Tan, Acta Mater 195 (2020) 433–445.
[5] Z. Guo, W. Sha, D. Vaumousse, Acta Mater 51 (2003) 101–116.
[6] Y. Zhang, D. Zhan, X. Qi, Z. Jiang, J. Mater. Sci. Technol. 35 (2019) 1240–1249.
[7] L.E. Samuels, Light Microscopy of Carbon Steels, ASM International, OH, 1999.
[8] Y. Wang, Y. Tomota, T. Ohmura, S. Morooka, W. Gong, S. Harjo, Acta Mater 184 (2020) 30–40.
[9] D. An, S.-I. Baik, Q. Ren, M. Jiang, M. Zhu, D. Isheim, B.W. Krakauer, D.N. Seidman, Mater. Charact. 162 (2020) 110207.
[10] D. Schryvers, P. Boullay, P.L. Potapov, R.V. Kohn, J.M. Ball, Int. J. Solids Struct. 39 (2002) 3543–3554.
[11] S. Morito, H. Tanaka, R. Konishi, T. Furuhara, T. Maki, Acta Mater 51 (2003) 1789–1799.
[12] A. Navarro-López, J. Hidalgo, J. Sietsma, M.J. Santofimia, Mater. Charact. 128 (2017) 248–256.
[13] G.Y.P. Medinaa, E.H. Delgadoa, A.F.M. Péreza, H.L. Ferreirab, Mater. Res. 20 (2017) 1161–1165.
[14] J.A. Taillon, C. Pellegrinelli, Y.-L. Huang, E.D. Wachsman, L.G. Salamanca-Riba, Ultramicroscopy 184 (2018) 24–38.
[15] F.J. Humphreys, Scr. Mater. 51 (2004) 771–776.
[16] A. Winkelmann, G. Cios, T. Tokarski, G. Nolze, R. Hielscher, T. Kozieł, Acta Mater 188 (2020) 376–385.
[17] F. Long, D. Kerr, G. Domizzi, Q. Wang, M.R. Daymond, Acta Mater 129 (2017) 450–461.
[18] R. Fialho Tomaz, D. Brandão Santos, K. Camey, R. Barbosa, M. Spangler Andrade, D. Pérez Escobar, J. Mater. Res. Technol. 8 (2019) 2423–2431.
[19] S.L. Shrestha, A.J. Breen, P. Trimby, G. Proust, S.P. Ringer, J.M. Cairney, Ultramicroscopy 137 (2014) 40–47.
[20] L. Ryde, Mater. Sci. Technol. 22 (2006) 1297–1306.
[21] M. Díaz-Fuentes, A. Iza-Mendia, I. Gutiérrez, Metall. Mater. Trans. A 34 (2003) 2505–2516.
[22] F.J. Humphreys, J. Microsc. 195 (1999) 170–185.
[23] B. Gaskey, L. Hendl, X. Wang, M. Seita, Acta Mater 194 (2020) 558–564.
[24] J. Gola, J. Webel, D. Britz, A. Guitar, T. Staudt, M. Winter, F. Mücklich, Comput. Mater. Sci. 160 (2019) 186–196.
[25] J. Gola, D. Britz, T. Staudt, M. Winter, A.S. Schneider, M. Ludovici, F. Mücklich, Comput. Mater. Sci. 148 (2018) 324–335.
[26] B.L. DeCost, E.A. Holm, Comput. Mater. Sci. 110 (2015) 126–133.
[27] M. Guillaumin, J. Verbeek, C. Schmid, in: 2009 IEEE 12th International Conference on, IEEE, 2009, pp. 498–505.
[28] A. Mignon, F. Jurie, in: Computer Vision and Pattern Recognition(CVPR), 2012 IEEE Conference on, IEEE, 2012, pp. 2666–2672.
[29] T. Okuyama, T. Gonsalves, J. Upadhay, in: 2018 International Conference on, IEEE, 2018, pp. 201–205.
[30] C. Liu, K. Chusap, Z. Li, Z. Chen, D. Rogers, F. Song, in: 2019 IEEE International Conference on, IEEE, 2019, p. 363.
[31] A. Rajkomar, E. Oren, K. Chen, A.M. Dai, N. Hajaj, M. Hardt, P.J. Liu, X. Liu, J. Marcus, M. Sun, P. Sundberg, H. Yee, K. Zhang, Y. Zhang, G. Flores, G.E. Duggan, J. Irvine, Q. Le, K. Litsch, A. Mossin, J. Tansuwan, D. Wang, J. Wexler, J. Wilson, D. Ludwig, S.L. Volchenboum, K. Chou, M. Pearson, S. Madabushi, N.H. Shah, A.J. Butte, M.D. Howell, C. Cui, G.S. Corrado, J. Dean, npj Digit. Med. 1 (2018) 1–10.
[32] Z. Che, Y. Liu, in: 2017 IEEE International Conference on, IEEE, 2017, pp. 1100–1109.
[33] A. Mogelmose, M.M. Trivedi, T.B. Moeslund, IEEE T Intell. Transp. 13 (2012) 1484–1497.
[34] Y. Wu, Y. Liu, J. Li, H. Liu, X. Hu, in: The 2013 International Joint Conference on, IEEE, 2013, pp. 1–7.
[35] S.M. Azimi, D. Britz, M. Engstler, M. Fritz, F. Mucklich, Sci Rep 8 (2018) 2128.
[36] F. Ajioka, Z.-L. Wang, T. Ogawa, Y. Adachi, ISIJ Int 60 (2020) 954–959.
[37] B. Ma, X. Ban, H. Huang, Y. Chen, W. Liu, Y. Zhi, Symmetry-Basel 10 (2018) 107.
[38] B.L. DeCost, B. Lei, T. Francis, E.A. Holm, Microsc. Microanal. 25 (2019) 21–29.
[39] M. Müller, D. Britz, F. Mücklich, Adv. Mater. Process 179 (2021) 16–21.
[40] P. Yang, R. Guo, P. Guo, Z. Fang, in: Proceedings 2011 International Conference on, IEEE, 2011, pp. 1465–1468.
[41] C. Hofer, S. Primig, H. Clemens, F. Winkelhofer, R. Schnitzer, Adv. Eng. Mater. 19 (2017) 1600658.
[42] N. Ibtehaz, M.S. Rahman, Neural Netw 121 (2020) 74–87.
[43] G. Litjens, T. Kooi, B.E. Bejnordi, A.A.A. Setio, F. Ciompi, M. Ghafoorian, J.A.W.M. van der Laak, B. van Ginneken, C.I. Sánchez, Med. Image Anal. 42 (2017) 60–88.
[44] O. Ronneberger, P. Fischer, T. Brox, in: Medical Image Computing and Computer-Assisted Intervention – MICCAI 2015, Springer International Publishing, 2015, pp. 234–241.
[45] Z. Chen, L. Deng, G. Li, J. Sun, X. Hu, L. Liang, Y. Ding, Y. Xie, IEEE T Neur. Net. Lear. 1 (2020) 348–362.
[46] N. Srivastava, G.E. Hinton, A. Krizhevsky, I. Sutskever, R. Salakhutdinov, J. Mach. Learn. Res. 15 (2014) 1929–1958.
[47] J.C. Duchi, E. Hazan, Y. Singer, J. Mach. Learn. Res. 12 (2011) 2121–2159.
[48] P. De Boer, D.P. Kroese, S. Mannor, R.Y. Rubinstein, Ann. Oper. Res. 134 (2005) 19–67.
[49] R.K. Yadav, Anubhav, Cogn. Syst. Res. 64 (2020) 191–199.
[50] J. Long, E. Shelhamer, T. Darrell, in: 2015 IEEE Conference on, IEEE, 2015, pp. 3431–3440.
[51] A. Baskaran, G. Kane, K. Biggs, R. Hull, D. Lewis, Comput. Mater. Sci. 177 (2020) 109593.
[52] X. Hu, X. Sun, K. Raghavan, R.J. Comstock, Y. Ren, Mater. Sci. Eng. A 780 (2020) 139176.
[53] F. Badkoobeh, A. Nouri, H. Hassannejad, H. Mostaan, Mater. Sci. Eng. A 790 (2020) 139703.
[54] M.D. Zeiler, R. Fergus, in: Computer Vision – ECCV 2014, Springer International Publishing, 2014, pp. 818–833.
[55] I. Díaz, A. Diez, A.A.C. Vega, in: G. Dorffner, H. Bischof, K. Hornik (Eds.), Artificial Neural Networks — ICANN 2001, Berlin , Heidelberg, Springer, 2001, pp. 443–449.
[56] Y.-F. Shen, R. Pokharel, T.J. Nizolek, A. Kumar, T. Lookman, Acta Mater 170 (2019) 118–131.